Optical Coherence Tomography: Principles and Applications of Microvascular Imaging

22

Beau A. Standish, Adrian Mariampillai, Michael K. K. Leung, and I. Alex Vitkin

Contents

B.A. Standish (✉) • A. Mariampillai
Department of Electrical and Computer Engineering, Ryerson University, Toronto, Canada
e-mail: standish@ee.ryerson.ca, a.mariampillai@ryerson.ca

M.K.K. Leung
Departments of Medical Biophysics and Radiation Oncology, University of Toronto, Toronto, Canada
e-mail: michaelkk.leung@utoronto.ca

I.A. Vitkin
Departments of Medical Biophysics and Radiation Oncology, University of Toronto, Toronto, Canada

Division of Biophysics and Bioimaging, Ontario Cancer Institute/University Health Network, Toronto, Canada
e-mail: Alex.Vitkin@rmp.uhn.on.ca

V.V. Tuchin (ed.), *Handbook of Coherent-Domain Optical Methods*,
DOI 10.1007/978-1-4614-5176-1_22,

Abstract

Microvascular detection and quantification with optical coherence tomography is an exciting and growing research field and is the topic of this chapter. Specifically, the fundamental principles of OCT microvascular imaging are described, encompassing phase-resolved and power-based methods, and the use of exogenous contrast agents. Representative biomedical applications of microvascular OCT imaging are presented, with emphasis on treatment monitoring and tissue response assessment. A discussion of outstanding challenges and future outlook concludes the chapter.

22.1 Introduction

A healthy vascular supply is essential for normal function in biological tissues, whereas anomalies in the vascular supply are associated with disease processes such as abnormal cellular proliferation in cancer [1], age-related macular degeneration [2], and atherosclerosis [3]. Of these examples, cancer represents one of the most diverse environments for neovasculature as the pathophysiology of solid tumors constantly recruits and develops new microvascular networks in a process called tumor angiogenesis. If these modified vascular networks can be identified early in the disease progression, then appropriate risk stratification/screening strategies may benefit patient management; further, therapies aimed at disrupting the neovascular supply, and monitoring the efficacy of this disruption, may enable more efficacious treatments.

Tumor vessels are chaotic, lack hierarchy, and exhibit abnormal spatial patterns and volumetric densities. Tumor endothelial cells lining its vessel walls also have different phenotypic properties compared to those in normal vasculature [4]. As a consequence, tumor vasculature has functional abnormalities such as unstable velocity and direction of blood flow, high vascular resistance, and structural fragility. Furthermore, flow is often erratic, displaying stasis or even reversal in certain vessels [5]. As there are such drastic differences between normal and tumor blood vessels, these may provide contrast mechanisms for the detection of cancer (potentially at its premalignant or early stage) along with monitoring strategies for developing and optimizing vascular-targeted therapies.

Clinical imaging methods such magnetic resonance imaging (MRI), computed tomography (CT), positron emission tomography (PET), and ultrasound (US) all have the ability to detect various aspects of tissue blood flow but lack the spatial resolution to directly image the microscopic vascular structures such as capillaries, venules, arterioles, or the lymphatic vessels. Therefore, the scope of this book chapter will focus on optical methods that can detect in vivo microvascular networks. Currently, vascular detection and assessment methods used for cancer prognosis largely rely on ex vivo microscopic examination of static vessel structures in resected tissue specimens. Following biopsy and fixation, vessels are stained, and metrics such as planar 2D microvessel density (MVD, used to assess

tumor angiogenesis) and 2D intercapillary distance (ICD, thought to indicate tumor oxygenation) are derived [6]. In several human tumor types, particularly breast cancer, these can serve as independent prognostic factors to predict relapse-free and overall survival in patients [7]. MVD can also be used to stratify patients for different treatment regimes and may be predictive of their response to chemotherapy [8]. One method to obtain these vascular metrics is by counting individual or clusters of endothelial cells lining the insides of the vessel walls. Usually, only regions with the highest MVD, or "hot spots," are analyzed on the purported basis that these areas are most biologically important [7].

This histological "gold standard" for microvascular assessment has many important flaws. It is disruptive and painful to the patient, suffers from poor sampling statistics associated with localized tissue excision, is limited to 2-dimension (2D) analysis of thin planar tissue slices, reports on vessel anatomy and structure, and is generally unable to provide useful information on blood flow physiology and or functionality. Furthermore, the counting process is laborious, somewhat subjective, and is prone to variations in the number of vessels highlighted by the staining process depending on the antibody used [9]. Hence, MVD and other vessel architectural metrics are difficult to use and incorporate into the existing patient management process supported by standard pathology services. These histologically derived detection methods have a major additional shortcoming in that they are not practical for continuous patient monitoring, as physical biopsy specimens are required. Therefore, there exists an extensive opportunity to develop new noninvasive in vivo imaging techniques to compliment biopsy for tissue microvascular detection, such as high-resolution optical imaging strategies to directly visualize microcirculation details. This represents a paradigm shift from the ex vivo, geometrical/anatomical assessment of the tissue microvasculature (as reported by histology) for tumor detection/diagnosis and therapy response, to that of in vivo physiologically relevant metrics of blood perfusion. Several promising in vivo optical techniques, such as diffuse correlation spectroscopy, confocal microscopy, laser speckle contrast imaging, and optical coherence tomography, are under development to detect and quantify microvascular blood flow. These and other promising novel approaches (e.g., photoacoustics [10, 11]) may assume a significant role in biomedicine through detection, quantification, and response monitoring of various pathologies with significant microvascular involvement.

22.2 Brief Overview of Optical Vascular Detection Methods and Representative Uses

Diffuse correlation spectroscopy (DCS) has been used in vivo to monitor the relative blood flow fraction (rBF) as a function of various treatment parameters in photodynamic therapy (PDT, see Sect. 22.5.2) in animal tumor models, with promising correlations to the biological endpoint of tumor growth delay [12]. The major components of a DCS system are a CW laser, a non-contact probe with multiple delivery and detector fibers, and a camera to collect the diffusely reflected

light [13]. Employing an optical switching methodology, the light is directed through each of the source delivery fibers in a consecutive manner, followed by collection via the detection fibers. The detected signal intensity fluctuations of the diffuse light are sensitive to the motion of tissue scatterers within the sampled volume of tissue for the particular excitation – detection fiber geometry – and hence can give a relative indication of blood flow within the interrogated volume of tissue. For example, Yodh et al. [12] have shown that PDT-induced changes in the DCS-derived rBF metric were predictive of the treatment response. Specifically, mice that exhibited a slower decline in the rBF during the PDT treatment went on to have slower-growing tumors. An advantage of this technique is that it can continuously and noninvasively monitor tissue blood flow, as the probes do not require contact with tissue. However, this technique has several disadvantages; for example, the overall size of the DCS distal probe implies that primarily only near-surface regions contribute to the detected signal. Moreover, DCS is a bulk tissue assessment tool, presenting its metrics averaged over the sampling volume. In other words, it lacks the ability to resolve localized regions of tissue blood flow, since the technique does not directly image or visualize the tissue microvasculature. This is potentially an important limitation: in vascular-targeted therapies, such as prostate PDT, for example, optimal monitoring techniques should be able to provide spatially resolved (laterally and in-depth) local vascular feedback for targeted pathology regions or for nearby organs at risk, such as sensitive urethral or rectal wall structures.

Confocal microscopy is a widely used optical microscopy technique for examining tissue that has been resected, preserved, and histologically stained to yield submicron resolution images, with the additional benefit of functional assessment via fluorescent markers. This technique is the gold standard for imaging ex vivo tissue microvasculature referred to earlier, where bloods vessels can be identified through the histochemical staining of vascular endothelial cells [14]. The functionality of vessels can be assessed using exogenous contrast agents that are injected into the circulatory system prior to tissue excision and fixation. In addition to its important ex vivo microscopy role, several attempts at its in vivo extension have been recently reported in the context of intravital microscopy and microendoscopy [15, 16]. There have been a limited number of in vivo preclinical animal models, where intravital multiphoton confocal microscopy (MPCM) has been used in conjunction with fluorescence vascular contrast agents (e.g., FITC dextran) to image the microvascular network [17, 18]. However, MPCM suffers from a number of drawbacks that severely limits this technology to preclinical imaging scenarios and will impede its potential clinical adoption: (1) MPCM is slow (e.g., a 5 mm $\times$ 5 mm region can take $\sim$1 h to image); (2) fluorescent dyes can be difficult to work with in a patient setting (safety and regulatory issues), and their leaking out of the vascular network makes longitudinal imaging difficult; and (3) the exquisite axial and lateral resolution (submicron level) comes at a cost of limited depth of penetration ($<$400 μm).

Laser speckle contrast imaging (LSCI) is another optical approach that was developed in the 1980s, where full-field tissue images are acquired by a camera,

obtaining a quick snapshot of the speckle pattern [19]. The surface region of tissue is then imaged over subsequent snapshots, where blood flow can be inferred from the calculated spatial and temporal statistics of the resultant speckle modulation pattern. The LSCI technique has matured over the last 20 years, with success in imaging blood flow in the skin and excellent potential for monitoring brain function in animal models. The former was one of the original clinical applications of LSCI [20], using it as a feedback mechanism to optimize the laser therapy of port wine stain [21].

Similar to DCS, one of the drawbacks of LSCI is the inherent lack of depth resolution. Despite this limitation, LSCI has demonstrated particular utility in imaging the brain, when a portion of the skull is thinned or removed in animal models. As the majority of the microvascular network of the brain is superficial, LSCI has been used to monitor the changes in cerebral blood flow to map the oxygenation of the brain following sensory activation [22]. Subsequently, LSCI imaging has become a very useful tool for stroke research and for monitoring cerebral blood flow changes in the ischemic brain tissue in several animal models [23, 24]. For example, LSCI was used to monitor the collateral blood flow during acute stroke in a rat, highlighting the potential benefits of identifying the presence of collateral blood flow in selecting appropriate poststroke therapies [22]. The LSCI technique is inexpensive and easy to implement, readily yielding. However, the advantage of LSCI's inherent camera-based quick full-field imaging is also a disadvantage: it has proven difficult to package the LSCI platform into intracavity, endoscopic, or interstitial imaging scenarios, limiting its range of potential clinical uses to readily reachable surfaces. This, in combination with the lack of subsurface-depth-resolved information, will likely limit its biomedical uses to near-surface and small animal imaging.

Optical coherence tomography (OCT) is a promising emerging imaging modality that overcomes several limitations of the above vascular detection techniques and will be the focus of this chapter. Specifically, OCT is portable and inexpensive, can obtain high-resolution depth-resolved topographic images, is sensitive to blood flow down to the capillary level, and has recently become commercially available, with demonstrated variety of clinical uses and successes (e.g., ophthalmology, as discussed below). Its major drawback is arguably its limited imaging depth (1–3 mm in most tissues), so care must be taken in selecting imaging scenarios where this penetration depth probes suitable tissue of interest (e.g., mucosal linings of various body cavities, intravascular plaque assessment, retinal imaging, and model studies in small animals). OCT is somewhat analogous to ultrasound, but instead of backscattered pressure waves, OCT measures backscattered photons. Interferometric detection is used, relying on coherence gating (thus the "C" in OCT) to obtain depth-resolved information, thereby avoiding the difficult task of directly measuring the time of flight of the backscattered light. Recent state-of-the-art OCT systems have demonstrated submicron spatial resolutions [25], allowing for the in vivo detection of subcellular features. Additionally, several OCT vascular detection approaches have been developed to move beyond structural imaging. We will now describe their scientific fundamentals along with selected illustrative examples of preclinical/clinical applications.

22.3 Microvascular Imaging with Optical Coherence Tomography

Over the past decade, there have been many advances in tissue microvascular imaging using OCT. Algorithms and techniques developed over this time period can be broadly divided into two groups: (1) those that attempt to quantify blood flow (e.g., velocity, direction) and (2) those that simply visualize microvasculature. (1) The majority of the techniques that attempt to quantify velocity, such as color Doppler imaging, are based on measuring the mean frequency shift induced by moving scatterers (red blood cells) across multiple A-scans [26, 27]. It is also possible to measure flow rates by examining speckle spatial frequencies in OCT intensity (B-mode) images [28]. However, this approach is only able to estimate the flow rate to within an arbitrary scaling factor. (2) On the other hand, the methods developed to only visualize, but not quantify, vascular flow measure the power (intensity) in the signal attributed to moving scatterers. These techniques include power Doppler, optical microangiography, intensity-modulated phase variance, and speckle variance [29–32].

To obtain an intuitive understanding of how these two different classes of measurement techniques are related, it is useful to consider the simple imaging scenario in which a planar reflector is moving with constant velocity in the direction of the optical axis. For frequency domain OCT, the measured signal from this target at time $t = 0$ and $t = \tau$ can be written as

$$I(0,k) = 2S(k)E_R a(z_1)\cos[2knz_1] \tag{22.1}$$
$$I(\tau,k) = 2S(k)E_R a(z_1)\cos[2kn(z_1 - v\tau)].$$

Here, $S(k)$ is the source spectrum, E_R is the light reflected from reference arm, $a(z_1)$ is the reflectivity of the plane reflector located at position z_1, n the index of refraction of the medium, and v the velocity of the planar reflector. These equations describe a translating set of fringes (i.e., sequentially obtained at offset lateral positions) in time for a frequency domain system. The basic principles of OCT Doppler detection employing a subset of the N A-scans acquired from the reflector at the depth z_1 are shown in Fig. 22.1.

The sampled signal traced out along the dashed black line (single k value) is termed the slow-time signal. Its mean angular frequency can be calculated from the power spectrum, $P(\omega)$, of the slow-time signal using

$$\varpi = \frac{\int \omega P(\omega) d\omega}{\int P(\omega) d\omega}. \tag{22.2}$$

This mean frequency $f = \varpi/2\pi$ of the slow-time signal is commonly referred to as the Doppler frequency, f_D, and can be related to the velocity of the moving plane reflector by

$$v = \frac{\lambda f_D}{2n}. \tag{22.3}$$

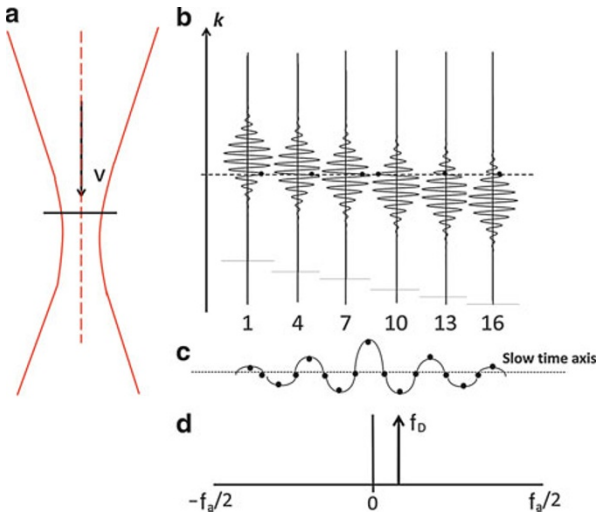

Fig. 22.1 Principles of OCT Doppler imaging. (**a**) A simple reflector propagating with a velocity v along the interrogating beam. (**b**) Subset of acquired fringes from the sample, the *green dashed line* representing the depth location of interest. The numbers label the sequential depth scans (referred to as A-scans). (**c**) The slow-time signal, with its sampled points at positions where the labeled A-scans in (**b**) intersect the *dashed green line* (points from additional A-scans also shown). (**d**) Power spectrum of the slow-time signal, where f_a is the A-scan rate of the OCT system

In the more general case where the reflector is moving at an angle θ with respect to the optical axis, the velocity is given by

$$v = \frac{\lambda f_D}{2n\cos(\theta)} \tag{22.4}$$

The Doppler frequency is most commonly measured through an autocorrelation approach, which calculates the phase shift between sequential A-scans, as discussed in the following section.

Alternatively, instead of measuring the frequency of the slow-time signal, one could also estimate the power in the slow-time signal corresponding to moving scatterers. This concept becomes the basis for power-based methods:

$$I_{PD} = \int P(\omega)d\omega. \tag{22.5}$$

In the idealized example of Fig. 22.1, all of the power is contained in the frequency band centered at f_D. In reality, the OCT field of view will encompass both moving (mostly blood) and stationary (mostly tissue) scatterers, and the power spectrum will have additional complicating features. A more accurate schematic of the slow-time power spectrum, although still idealized, is shown in Fig. 22.2.

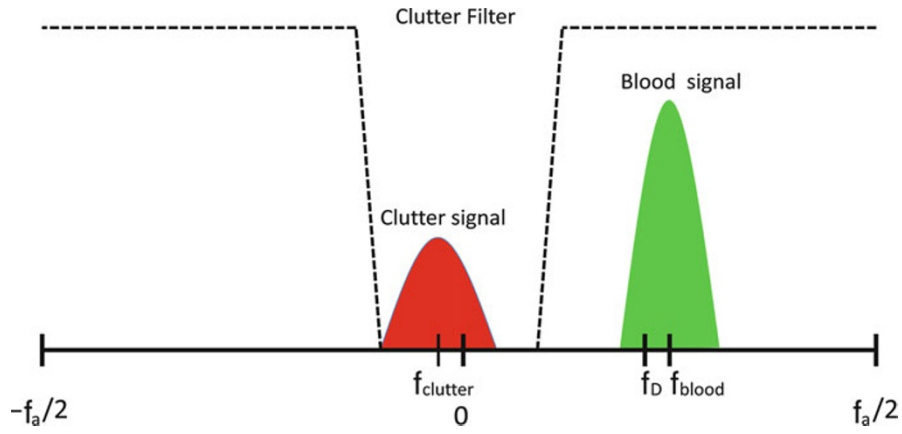

Fig. 22.2 Schematic power spectrum of slow-time signal from B-mode image of tissue. The moving blood signal is centered about f_D, and the tissue clutter signal is centered about $f_{clutter}$. If the background tissue is truly stationary, the latter is centered about zero frequency. Often, there is also bulk tissue motion, causing a shift in the $f_{clutter}$ distribution away from the baseband. In the illustration above, the tissue is moving away from the interrogating beam, hence the negative frequency location of the clutter signal. The *dotted lines* represents an idealized clutter rejection band-stop filter that suppresses the clutter signal frequencies, in order to generate accurate Doppler images representative of tissue blood flow

The spectrum now has two components: (1) tissue scatterers, generally termed clutter, with mean frequency $f_{clutter}$ and (2) moving scatterers in the blood with mean frequency f_{blood}. As described in the figure caption, the clutter signal arises from stationary tissue but can also have a bulk tissue motion component. In the presence of clutter, an estimate of the mean frequency f_D, using (22.1), (e.g., as needed for color Doppler imaging) will be distorted by the presence of the stationary or slowly moving tissue signal. However, this distortion is generally negligible for mean frequency measurements, as the OCT voxel size ($\sim$10 μm × 10 μm × 10 μm) is small enough that it can be considered to be fully filled with blood or not at all (i.e., both clutter and blood signals are unlikely to be present in the same voxel). On the other hand, estimation of the power in these clinically relevant situations must account the presence of the clutter spectrum, with a band-stop filter (also referred to clutter filters or wall filters in the ultrasound literature) applied to remove it (dotted line in Fig. 22.2), before the power in the remaining blood signal can be accurately calculated and displayed. Thus, to accurately estimate the slow-time signal frequency and power, a number of different factors must be considered to yield optimized blood flow detection as follows:

1. The number of slow-time samples used in the estimates and the time between successive samples
2. Finite displacement between adjacent A-scans resulting from lateral scanning schemes (which induce broadening of the slow-time signal spectrum)
3. The presence of static or slowly moving scattering structures (tissue clutter)

In the next two sections, the implications of these factors on the measurement of the mean frequency and power will be discussed.

22.3.1 Phase-Resolved Methods

When acquiring two A-scans taken at the same position at slightly different times, the slow-time (Doppler) frequency can be estimated by measuring the phase shift, in the direction of the optical beam, which is induced by the scattering particles using autocorrelation analysis. To perform the autocorrelation analysis, two or more consecutive A-scans are acquired from approximately the same location. Typically, using a larger number of samples (e.g., $N = 16$ or 32) improves the estimate of the phase shift, where N is referred to as the packet length. The frequency of the slow-time signal can then be related to the phase shift via the equation

$$f_d = \Omega f_a, \tag{22.6}$$

where Ω is the measured phase shift and f_a is the A-scan rate (assuming a linear change of phase with time) over the time interval $\Delta t = 1/f_a$.

In practice, the Doppler frequency can be estimated using the Kasai velocity estimator [33]

$$f_d = \frac{f_a}{2\pi} \arctan\left\{ \frac{\frac{1}{M(N-1)} \sum_{m=1}^{M} \sum_{n=1}^{N-1} I_{m,n+1} Q_{m,n} - Q_{m,n+1} I_{m,n}}{\frac{1}{M(N-1)} \sum_{m=1}^{M} \sum_{n=1}^{N-1} Q_{m,n+1} Q_{m,n} + I_{m,n+1} I_{m,n}} \right\}. \tag{22.7}$$

Here, I and Q are the in-phase and quadrature components of the demodulated detector signal, and m is the axial averaging index. The index n represents adjacent A-scans in the lateral direction, in which the autocorrelation analysis takes place. This estimator provides a computationally efficient way to estimate the Doppler shift over a packet length of N A-scans [26]. Figure 22.3 shows an example of structural and color Doppler imaging from the heart of *Xenopus laevis* tadpole employing this phase-resolved flow detection technique. Due to the limited A-scan frequency of the OCT system used in this experiment (16 kHz), aliasing occurred in the spiral valve of the truncus arteriosus (TA), where detected frequencies were greater than the aliasing frequency of $f_a/2$ (from [34]).

A number of factors influence the sensitivity (minimum measurable phase shift and thus minimum detectable blood velocity) of a Doppler OCT system. Most important is the influence of the structural signal-to-noise ratio (SNR) on the Doppler noise floor. To estimate the SNR-limited Doppler noise floor, consider the simple theoretical model, which defines the SNR as

$$SNR = \left(\frac{\overrightarrow{|E|}}{|\vec{n}|} \right)^2. \tag{22.8}$$

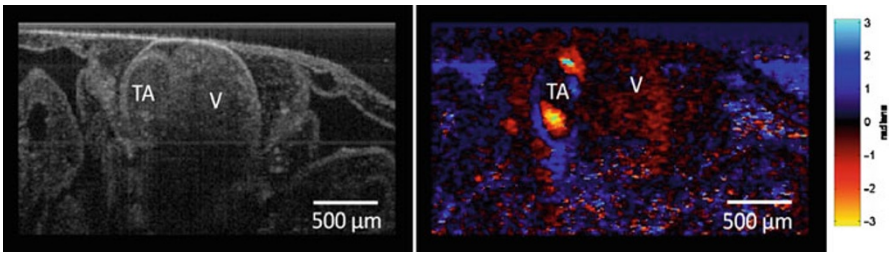

Fig. 22.3 Structural and Doppler flow image showing blood being ejected out of the truncus arteriosus (TA) in the *Xenopus laevis* tadpole heart. To the right of the truncus arteriosus is the ventricle (V)

Here, $\vec{n}$ is a random noise vector and $\vec{E}$ is the reflected electric field at the detector. In the regime where high *SNR* is observed ($|\mathrm{E}| >> |\mathrm{n}|$), the standard deviation of the phase shift between two A-scans is given by [29]

$$\sigma_{\Delta\varphi} = \frac{1}{SNR^{1/2}}. \tag{22.9}$$

The SNR-limited phase noise is the lowest phase shift that can be measured between two A-scans. For optimal Doppler detection, the system should always be operating as close to this threshold as possible.

Another important factor that contributes to the DOCT noise floor is the fact that the majority of OCT systems use only a single linearly scanned beam to generate B-mode images; in other words, consecutive A-scans are not sampling exactly the same spatial location. This introduced lateral displacement between each A-scan during B-mode imaging, which increases the Doppler noise floor (broadening of the clutter signal spectrum) [26]. Standard protocols to minimize these effects include extensive lateral oversampling. However, this reduces the effective frame rate of the system [35, 36]. A related noise issue is that of physiological motion (sometimes referred to bulk tissue motion), which can shift the center frequency of the clutter spectrum. This can make it very difficult to interpret color Doppler images, due to large bulk phase shifts that are superimposed on the Doppler signals. A number of techniques have been developed to address this problem, where two of the most commonly used include (1) the simple subtraction of the mean phase shift from each line in the Doppler image and (2) the histogram rejection technique [35, 37].

It is important to note that ongoing technical advances in Fourier-domain OCT systems (faster swept sources and/or spectrometers) for volumetric OCT imaging can actually be counterproductive for phase-resolved Doppler detection, as these blood flow measurement schemes require phase buildup between successive A-scans. Therefore, as the time between consecutive A-scans becomes smaller (inversely proportional to the A-scan rate of OCT system), there is less time for a measurable phase difference to be measured. In the best-case scenario, when the

phase noise floor remains constant, as the A-scan rate increases, there is a linear reduction in the minimum detectable velocity. This can be overcome by a proportional increase in the packet length N (number of A-scans used in the Kasai, or other, velocity estimator). However, this slows the imaging frame rate, diminishing the advantages afforded by increased A-scan rates.

Typical minimum detectable velocities for phase-resolved methods lie in the range of 100–500 μm/s. These values are directly dependent on the imaging system and sample characteristics for signal detection. Physiologically, this lower limit implies phase-resolved methods are able to detect flow in larger arterioles and venules, but smaller vessels and capillaries will not be detected. Although the phase-resolved methods suffer from a variety of complication as mentioned above (along with additional complications arising from Doppler angle requirements and aliasing), phase-resolved methods do provide a robust method of calculating blood flow velocity in OCT.

22.3.2 Power-Based Methods

Power Doppler OCT (PD-OCT) imaging was first applied to time-domain OCT systems [26, 38]. PD-OCT is based on first filtering out the stationary or slowly moving tissue component (clutter) of the slow-time power spectrum using a high-pass filter and subsequently quantifying the remaining signal intensity. In the idealized case shown in Fig. 22.2, the clutter rejection filter centered at zero frequency has sufficient bandwidth to remove the clutter signal (centered at $f_{clutter}$), while leaving the Doppler signal from blood (centered at f_{blood}) unaffected. In practical in vivo imaging scenarios, it is crucial to match the clutter filter characteristics to that of the clutter signal in order to obtain sufficient rejection of the tissue clutter components. This filter matching is complicated by the same factors that degrade color Doppler imaging: low SNR and the use of a linearly scanned beam that broadens the clutter spectrum. Therefore, a broader bandwidth clutter rejection filter must be used, which inevitably removes a finite fraction of the low velocity blood signals. Bulk tissue motion shifts the center of the clutter spectrum in a motion-dependent fashion, necessitating the use of adaptive filters which compensate for these effects [39] or the use of very broad band filters. Finally, as in the case of phase-resolved methods, the ever-increasing OCT A-scan speeds afforded by faster lasers and spectrometers allow very little time for the slow-moving blood spectrum to separate from the clutter spectrum, resulting in partial removal of the blood spectrum signal by the clutter signal filter.

Recently, a technique known as optical angiography (OAG) has also been developed for frequency domain OCT [30]. This technique is similar to PD-OCT except that the filtering of the tissue clutter, from the slow-time power spectrum, occurs in the frequency domain via a Hilbert transform [30]. Overall, the greatest benefit of power Doppler and OAG imaging, compared to phase-sensitive techniques, is that averaging multiple lines and frames from the same location (an approach known as persistence in ultrasonography) increases the system's

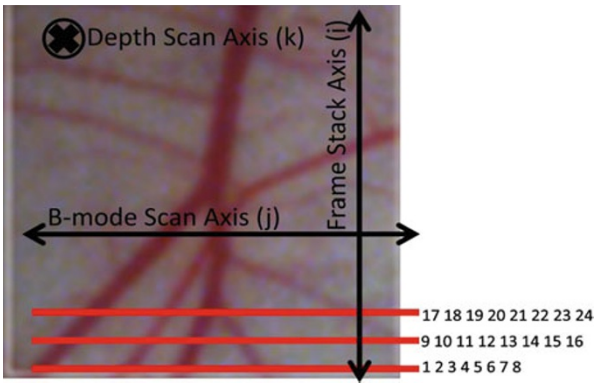

Fig. 22.4 Interframe scanning pattern used to perform high-sensitivity vascular imaging with techniques such as speckle variance (SV) OCT. Acquisition of multiple B-mode frames at each location (indicated by their numerical index on the *right* of the figure, at a representative B-mode location) minimizes decorrelation of static structures, thus maximizing vascular contrast

sensitivity to smaller vessels. Additionally, PD-OCT imaging does not suffer from aliasing and angle dependence as seen in CD-OCT, making it easier to interpret for real-time application where flow velocity is not needed. PD-OCT can also be color-coded to indicate the directionality of flow. This is accomplished by first applying the clutter filter and then applying a filter that either removes all positive components or negative components resulting in two separate power Doppler images – one that displays only positive components of the power spectrum and one that only displays the negative components. These two images are typically color-coded red and blue, respectively, and merged into a single directional power Doppler image [40].

However, even with the use of large amounts of averaging, the smallest vessels cannot be detected using standard PD-OCT techniques, as the current OCT A-scan rates (on the order of tens of kHz) do not allow enough time for the blood flow spectrum to separate from the low-frequency tissue clutter spectrum. An elegant solution is to move away from intraframe measurements (where the slow-time sampling frequency is f_a) to interframe techniques (axis i in Fig. 22.4) This increases the integration time between successive measurements, allowing the blood scatterers to move sufficient physical distances to uncouple f_D signals from $f_{clutter}$ signals.

This idea forms the basis for OCT techniques such as ultrahigh-sensitivity OMAG (UHS-OMAG) [41], phase variance [29], intensity-modulated phase variance [31], and speckle variance (SV) [32]. In these techniques, where the interframe time between measurements becomes large, the blood component of the slow-time power spectrum (now in the frame direction) becomes uniformly distributed in frequency, as shown in Fig. 22.5. This uniform distribution of phases arises from complete decorrelation of the OCT signal, on the order of the interframe timescale.

Clutter signals can now be filtering out using a high-pass filter, leaving the power associated with moving blood scatterers to generate highly sensitive vascular maps.

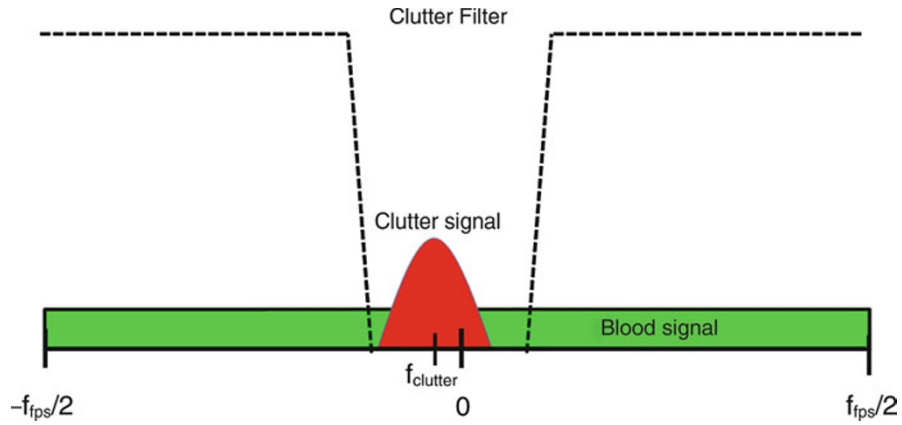

Fig. 22.5 Power spectrum of slow-time signal taken in the frame stack direction. The effective sampling rate now becomes the frame rate of the system in frames per second (fps)

For example, the algorithm for generating speckle variance images requires calculating the variance of pixels from a set of N B-mode images (here, N is known as the gate length), acquired from the same spatial location using the equation

$$SV_{ijk} = \frac{1}{N}\sum_{i=1}^{N}\left(I_{ijk} - \frac{1}{N}\sum_{i=1}^{N} I_{ijk}\right)^2. \tag{22.10}$$

Here, i, j, and k are indices for the frame, transverse, and axial pixels, respectively, and I is the corresponding pixel intensity value. For clarity, a schematic representation of a typical data set and pixel indices is shown in Fig. 22.6.

Figure 22.7 demonstrates a highly sensitivity color-coded vascular projection map of a tumor obtained with the above SV-OCT approach. Features closest to the surface have been encoded as green yellow, while deeper features are encoded with orange red, and the transparency of each pixel is determined by the speckle variance intensity [42]. As seen, these blood flow detection techniques now have the ability to directly visualize the 3D capillary bed in vivo to a depth of ~1 mm. The next section discusses further improvements in the robustness of this approach (especially in the presence of tissue motion) and imaging depth (potentially with the introduction of exogenous contrast agents).

The recent development of interframe power-based blood flow detection techniques has enabled hitherto unavailable in vivo sensitive detection of the entire vascular network throughout several millimeters of tissue. These new approaches, in combination with high A-scan rate Fourier-domain OCT systems, have yielded imaging tools that are capable of providing 3D morphological and vascular data sets in mere seconds. This unprecedented ability to provide volumetric vascular perfusion maps in vivo may have widespread preclinical and clinical applications, ranging from model small animal studies to wound healing to disease detection to

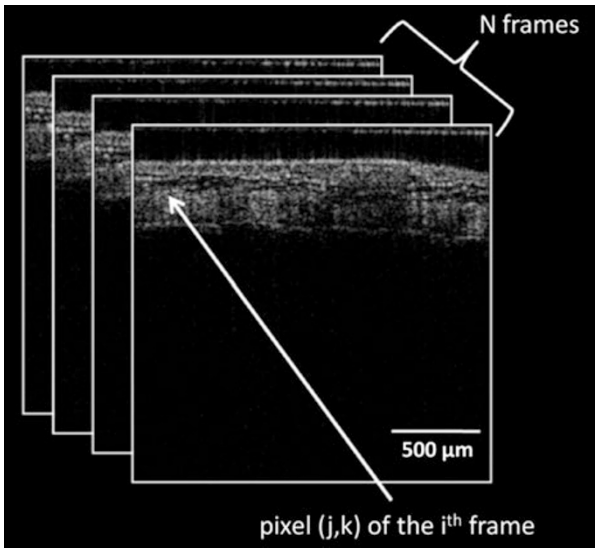

Fig. 22.6 Schematic representation of an acquired speckle variance data set of *N* frames, and the corresponding indices used to label the frame (*i*), transverse pixel location (*j*), and the axial pixel location (*k*)

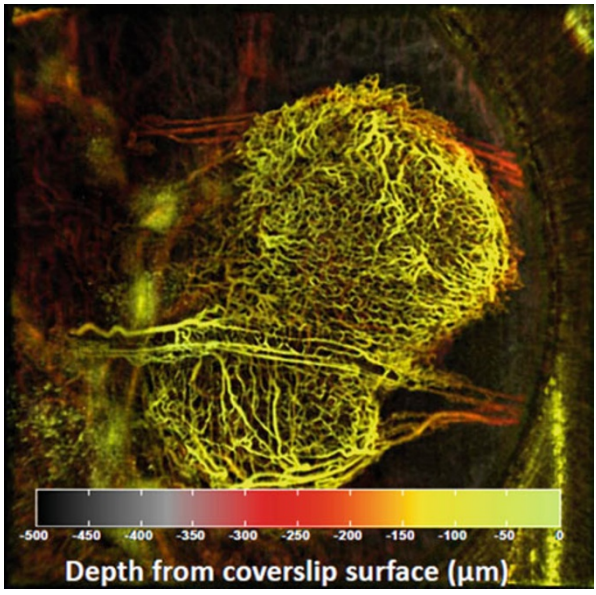

Fig. 22.7 Depth-encoded color projection image of 9L gliosarcoma tumor imaged 9 days after implantation in the dorsal skinfold window chamber model. Features closest to the coverslip are encoded with *green yellow*, while deeper features are encoded with *orange red*. The transparency of a pixel is determined by the speckle variance intensity. The image shows a significant amount of intratumoral microvascular heterogeneity [43]

treatment monitoring/optimization. As with all imaging modalities, each of these specific vascular detection schemes has their advantages and disadvantages, and the researcher or clinician must take great care in choosing a vascular detection scheme that is optimal for the specific application in question.

22.4 Contrast Agents to Improve Microvascular Detection

The OCT vascular detection techniques described above are based on Doppler shift, power Doppler, or speckle modulation and inherently assume the imaging background is essentially stationary, and that the only moving components are due to the presence of blood (either due to convective flow or due to natural Brownian motion even in the absence of flow as in the case of speckle modulation). Thus, the motion of the scatterers in blood is the overarching source of vascular contrast in OCT. In some cases, however, it may be advantageous if additional exogenous contrast can be localized in the vasculature, in order to better reject background (nonvascular) signals and decrease the reliance on the motion detection algorithm. Vascular contrast-enhancing agents are present in many other biological imaging modalities, making feasible the detection of vascular network, and recognizing regions of altered perfusion. They include iodinated agents in computed tomography, gadolinium in magnetic resonance imaging, and microbubbles for ultrasound. In optical imaging, a prevalent modality that relies on contrast agents is fluorescence imaging. A wide variety of fluorescently tagged molecules are used in confocal and multiphoton microscopy. One common vascular detection method involves the use of fluorescently tagged high molecular weight Dextran, which acts as a blood pooling agent and has been successfully used to diagnose vascular anomalies in the eye [44]. However, one of the primary drawbacks of fluorescence imaging for clinical applications is the limited depth of penetration. The use of contrast agents for OCT has the potential to enable high specificity of the imaging target, with an order of magnitude increase in imaging depth. However, a confounding factor to this potential for OCT deep vessel detection is that fluorescence is an incoherent process and is therefore unsuitable for OCT. Therefore, OCT must rely on actual changes in the (scattering and absorption) optical properties of the tissue to be imaged [45].

One potential mechanism for enhanced vascular contrast is thus to utilize agents with strong scattering or absorbing properties that can be localized in the blood. The following section discusses strategies to enable contrast-agent-enhanced vascular detection. Note that contrast agents for OCT imaging extend far beyond vascular imaging, where developments have been primarily focused on the detection of cellular biomarkers. Interested readers are referred to a review by Yang [46].

There are many commercially available near-infrared (NIR) absorbing dyes, which can alter the spectral properties of an imaging target within localized regions. The NIR dye indocyanine green, for example, has been FDA-approved and has found applications in ophthalmic angiography [47]. NIR dyes may be used as a contrast agent when combined with spectroscopic OCT, which can probe the spectral information of a sample [48, 49]. Dyes that have absorption peaks that are off-centered from the center wavelength of the OCT light source are chosen. Their presence causes a regional shift in the spectrum of the backscattered light where they are located. This shift can be detected using spectroscopic OCT, where the concentration of the dye may be determined by the amount of spectral shift from the

center wavelength of the light source. This has been successfully applied to the imaging of the vascular bundles of a celery stalk [50].

Microbubbles and microspheres are another type of contrast agent, relying on scattering alterations, that could potentially be utilized for vascular detection using OCT. Gas-filled microbubbles are highly scattering due to the large index of refraction mismatches that they create in tissue. They may also find applications for combined OCT and ultrasound imaging. Barton et al. demonstrated the OCT detection of phospholipid-coated perfluorobutane microbubbles in the femoral vessels of a mouse hind limb [51]. Other scatterers with refractive indices that are significantly different from tissue, such as gold and iron oxides, have also been encapsulated in microspheres for use as contrast agent in OCT [52]. However, an inherent difficulty with using either strong absorbers or high scatterers as contrast agent for OCT is that the biological tissues themselves generate a large range of backscattered signal. Combined with the presence of speckle, this makes differentiation of intrinsic contrast from an exogenous probe difficult, based on intensity alone. This may help explain the rather subtle improvements in vascular detection using microbubbles reported by Barton et al. [51].

To enhance the separation of contrast agents from the tissue background signal, it is possible to use a dynamic modulation method by observing the changes between a pair of images (B-mode) or between adjacent depth profiles (A-scans), while the absorbing or scattering properties of the contrast agent are altered. That is, a baseline acquisition is performed, the properties of the contrast agent are modified, and then a second acquisition is taken. The difference between the two B-mode images (or two A-scans) can be used to identify the location of the contrast agents. For example, methylene blue has a modifiable absorption peak that can be changed from 650 nm at ground state to 830 nm at an excited state by optical pumping. Difference images can be obtained by turning the pump on and off, as has been demonstrated by Rao et al. in what they termed "pump-probe OCT" [53]. The main difficulty with using methylene blue is its short excitation lifetime, requiring high pumping light intensity to allow a sufficient time window for image acquisition. Other molecules with longer transition times, such as phytochrome A, have also been explored [54]. Another modulated contrast agent is that of ferromagnetic particles. In magnetomotive optical coherence tomography [55], magnetic nanoparticles are mechanically modulated with an external magnetic field during OCT imaging. Background rejection is accomplished by performing an additional scan when the magnetic field is off. In principle, these modifiable contrast agents could be encapsulated within engineered microspheres to remain within vasculature. Alternatively, surface modifications could be performed on the microspheres to label diseased blood vessels as markers for arthrosclerosis or tumor angiogenesis [52]. These exogenous contrast agents for OCT have yet to become widely used or widely available to the OCT research community. Although signal improvement has been demonstrated, the inherent physiological implications and associated toxicities of these contrast agents remain unknown. Extensive preclinical testing is required prior to their acceptance as a technique to improve the viability of contrast-enhanced vascular OCT.

22.5 Representative Applications

22.5.1 Vascular OCT for Retinal Assessment

Mutation in the vascular network of the retina has been associated with various diseases including vascular occlusion disease, diabetic retinopathy, and glaucoma. Therefore, an opportunity exists to quantify the relative or absolute blood flow pattern of the retina as a way to gain a physiologically relevant understanding of these retinal diseases. Quantitative imaging of blood vessels, via color Doppler OCT, was first reported in 1997 [56, 57] and extended to retinal imaging by Yazdanfar et al. [58] in 2000. This concept of using the inherent blood flow as a contrast mechanism was employed to differentiate the stationary tissue from the moving red blood cells and to visualize the morphology of the blood vessels in the ocular fundus and is now termed optical coherence angiography (OCA) [59]. With recent advances in computer hardware and an increase in the A-scan rate of OCT systems, three-dimensional (3D) scans can now occur at multiple times per second, where the vascular information can be used to differentiate between retinal and choroidal vascular networks. Although fluorescein angiography (FA) is still the gold standard for vascular detection in the eye, recently developed inherent-contrast OCT blood detection techniques such as speckle variance, phase variance, and optical microangiography have the potential to replace FA as the accepted standard of care in the near future.

OCT is in fact becoming a standard of care for many ophthalmic diseases, and many ocular OCT studies have been reported. This has translated to and increased use of microvascular OCT imaging in the eye [60, 61]. For example, a recent Doppler OCT pilot study by Wang et al. [62] has demonstrated how ocular blood flow characteristics in retinal and optic nerve diseases could be used to stratify patients with and without disease. Subjects were subdivided into five groups – normal, glaucoma, nonarteritic ischemic optic neuropathy (NAION), diabetic retinopathy (PDR), and branch retinal vein occlusion (BRVO) – and their blood flow was detected and quantified, via the Doppler OCT velocity profiles, in a regions around the optic nerve head. It was found that the total retinal blood flow in normal patients averaged 47.6 ± 5.4 μL/min, whereas eyes with glaucoma (34.1 ± 4.9 μL/min), NAION (28.2 ± 8.2 μL/min), or PDR (15.8 ± 10.1 μL/min) had a significantly decreased blood supply ($P < 0.001$). In addition, there was a statistically significant correlation between the loss of normal blood flow in the eye and visual field loss in glaucoma patients ($P = 0.003$). This is but one example demonstrating how Doppler OCT retinal blood flow imaging can help identify and quantify diseases of the posterior chamber of the eye.

As OCT blood flow detection algorithms and techniques continue to be validated by preclinical and clinical research, several imaging and workflow advantages may allow these techniques to assume routine use in the clinic. These advantages include inherent (endogenous) vascular contrast without the need for exogenous contrast agent injection (e.g., fluorescein), no need for surface contact (cf. ultrasound), and OCT's ability to yield coregistered high-resolution morphological information and sensitive blood flow detection maps simultaneously.

22.5.2 Vascular OCT Monitoring of Photodynamic Therapy

Photodynamic therapy (PDT) is a non- or minimally invasive treatment that combines the effect of three nontoxic agents – photosensitizer, oxygen, and light – to produce a cytotoxic photochemical reaction. PDT is approved for treating a variety of solid tumors, dysplasias, and other oncologic and nononcologic pathologies [63, 64]. Several advantages of PDT as an oncotherapy include ability to preferentially target tumor while sparing adjacent normal tissues (owing to selective accumulation of photosensitizer and focal light irradiation strategies), reduced systemic phototoxicity using recently developed photosensitizers, ability to target either cellular or vascular tumor compartments, good cosmesis outcome (owing to sparing of the connective tissue and stroma), and lack of treatment resistance buildup (allowing for retreatments as necessary to improve response). Some disadvantages of PDT include systemic photosensitivity with previous generation of photosensitizers, inability to treat large tumors (related to limitations imposed by light propagation in tissue), overall complexity of the treatment (correct mixture of light, drug, and oxygen "doses"), and the need for a viable blood supply to ensure continuous oxygenation (which can prove difficult in a hypoxic tumor environment [65]).

When the photosensitizer is excited to a higher energy state by the PDT treatment light source, it can return to its ground energy level via nonradiative relaxation, fluorescence, or through an intermediate triplet state. It is this triplet state which is of most interest to the PDT effect, as the photosensitizer can undergo a type 1 or type 2 reaction. The type 2 reaction is considered to be the main cytotoxic PDT path leading to cell death [66], where the photosensitizer reacts with molecular oxygen to produce singlet oxygen [67]. As the singlet oxygen reacts with the tissue, cell destruction can occur via plasma membrane damage [68], bleb formation [68], reduction of active transport [69], depolarization of the plasma membrane [70], and cell lysis [65]. DNA damage has also been implicated in PDT, often mitochondrial and not nuclear, owing to the details of photosensitizer subcellular localization; unlike the mode of damage of ionizing radiation, however, the induced DNA base oxidative damage, strand breaks, and cross-links may be such that the damage is sublethal [71, 72].

In addition to (or perhaps instead of) cellular damage, tumor vasculature is also an attractive target during PDT, as the tumor environment requires a functional vascular system for the delivery of nutrients and for removal of toxic wastes associated with cellular metabolism of its rapidly proliferating cells. The tumor vasculature is significantly different from normal vasculature in both vessel architecture (tortuosity, irregular branching, lack of basement membrane in endothelial cells) and function (e.g., blood pooling, increased vessel permeability, perfusion) [73]. These differences provide a potential framework for preferentially targeting tumorous vasculature to disrupt or modulate vessel architecture/function, while limiting damage to normal vascular tree. An important benefit of vascular targeting, when compared to cellular targeting, is that not all endothelial cells need to be affected to disrupt tumor vascular function. Instead, damaging a single endothelial cell or small section of a blood vessel may induce catastrophic results, as thousands

of tumor cells may die since they were dependent on that single vessel section for their blood supply [74].

These PDT vascular impairment effects are complex and dynamic, but potentially useful; as such, they may be monitored, quantified, and perhaps optimized in real time via OCT. The vascular changes, if measurable, can offer a metric for quantifying the biological response of PDT, further elucidating its mechanisms of action and providing an early assessment of therapeutic efficacy. This may overcome some of the PDT dosimetry challenges and provide potential feedback information for therapy improvement and individualization.

OCT's ability to simultaneously image tissue structure and blood flow information is very promising for biomedical applications and is well suited for monitoring the vascular changes associated with PDT treatments. Doppler OCT (DOCT) is capable of producing high-resolution structural images while also acquiring blood flow characteristics at the microcirculation level. However, due to the shallow penetration depth of OCT (1–3 mm in scattering tissues), new technologies are needed to obtain DOCT images of deeply situated tissue for clinical applications such as prostate or brain cancer.

Yang et al. [75] first demonstrated the feasibility of using a needle-based OCT probe to minimally invasively image the microstructure and microvasculature of hamster leg muscle. Note that this approach does not improve the OCT imaging depth of 1–3 mm per se but rather enables its placement anywhere in 3D space (via a minimally invasive high-gauge needle, under radiologic guidance). This design was miniaturized (~400 μm diameter OCT probe) and used in several follow-up studies to monitor and quantify PDT in preclinical animal studies under varying treatment conditions. Standish et al. [76] demonstrated that interstitial (IS) DOCT was able to detect and monitor microvascular changes during and post-PDT, deep within the tumor in real time, by providing quantitative differences in the vascular response to varying irradiance rates. This study monitored dynamic changes in vascular blood flow and defined a new quantitative metric called the vascular shutdown rates. This IS-DOCT metric was then used by Standish et al. [77] to predict the biological endpoint of tumor necrosis after PDT treatment in a Dunning prostate tumor rat model. Figure 22.8 demonstrates typical blood flow detection images throughout a PDT treatment and corresponding changes in the vascular index. Note only a couple of vessels have been highlighted in Fig. 22.8a for ease of displaying the detected blood flow.

Figure 22.9 demonstrates the PDT-induced vascular shutdown within the treatment region of multiple rats. A resonable correlation ($R^2 = 0.72$) between the percent tumor necrosis at 24 h post treatment and the vascular shutdown rate was observed slower vascular shutdown rate corresponded to higher treatment efficacy (larger volume of tumor necrosis).

These results demonstrate the potential for clinical measurements of the vascular effects of PDT via Doppler OCT, laying the groundwork for further work to improve vascular detection along with new imaging protocols and platforms for detecting and quantifying tissue microvascular network including the capillary bed [32, 34, 42].

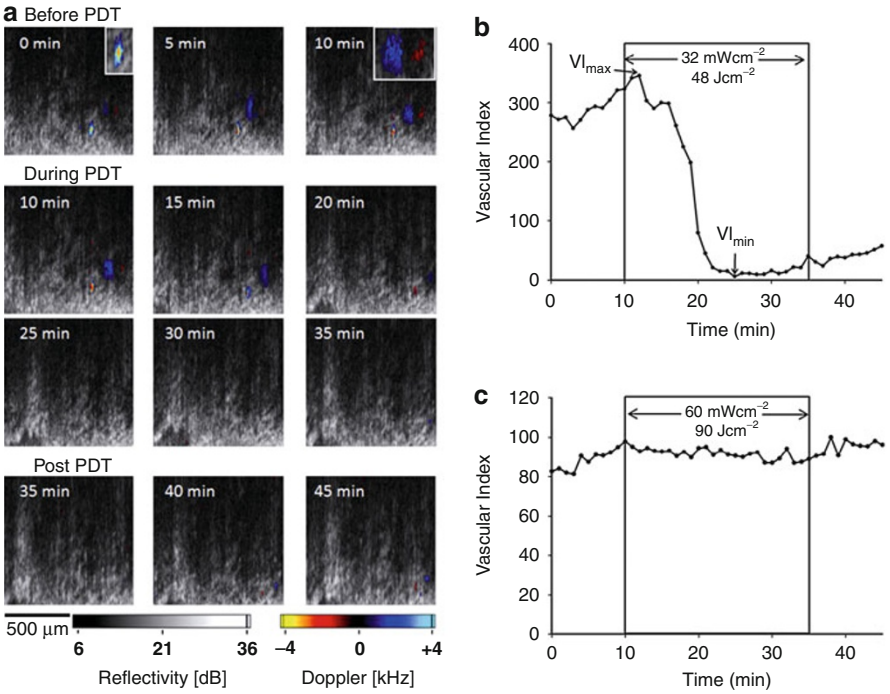

Fig. 22.8 Photofrin-mediated PDT, treatment time = 25 min. (**a**) IS-DOCT imaging sequence of color Doppler blood detection overlaid onto structural OCT images before, during, and post-PDT treatment. The inserts are 2× magnifications showing aliasing (0 min) and counterpropagating flows (10 min). (**b**) Vascular index VI as a function of time in a single animal showing the vascular shutdown during PDT light exposure and the definitions of VI_{max} and VI_{min}. (**c**) Control animal (light, no photosensitizer). Fluence rates and fluence listed in (**b**) and (**c**) are subsurface values at the depth of the IS-DOCT probe

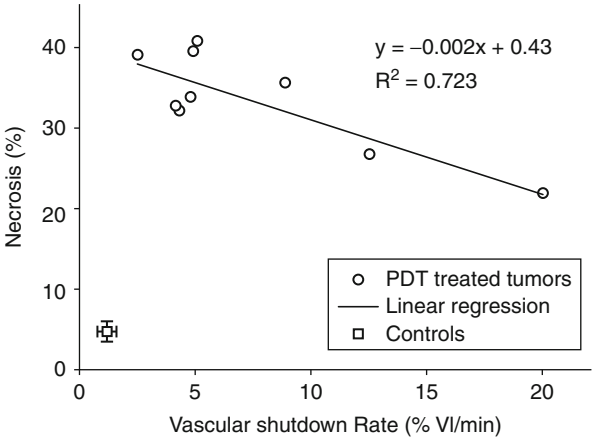

Fig. 22.9 Correlation between percent tumor necrosis and DOCT flow reduction rate in PDT-treated rats carrying Dunning prostate tumor xenografts. PDT-treated group showed a marked and a statistically significant ($R^2 = 0.723$) decrease in PDT treatment efficacy with the increased rate of vascular shutdown. Vascular index VI is a quantification of the relative blood flow fraction detected in Doppler OCT images

22.5.3 Vascular OCT in a Murine Window Chamber Model

Window chamber models for visualizing tissue development in vivo have been established since the 1920s [78]. In this approach, surgery is performed at the site of interest to implant an optically transparent window that allows for direct intravital imaging of otherwise inaccessible regions. The rabbit ear chamber, cranial chamber, dorsal skinfold chamber (DSWC), and other body organ windows (such as the kidney) have been demonstrated for different research areas [79]. All these models provide long-term (days, weeks, months) intravital observation of the organ of interest using high-resolution optical microscopy. The advantages of repeated longitudinal imaging studies in a well-controlled in vivo environment are beneficial to tumor implantation and development, controlled manipulation, disease treatments, and multimodality assessments and are highly beneficial for preclinical studies. The DSWC in particular has been used to study the microvasculature, with applications ranging from the studies of perfusion to monitoring various transplanted cells or tissues in the chamber to spatio/temporal quantification of responses to various treatments.

Figure 22.10a shows an example of a DSWC Swiss nude mouse commonly used for preclinical research. The model is convenient for DSWC implantation as the mouse is nude, avoiding the need for hair removal and skin irritation; its suppressed immune system permits the growth of various human xenografts tumor cell lines. The DSWC allows for direct observation of the cells, connective tissues and blood vessels of the normal dorsal skin environment, and, importantly, implanted tumor. Figure 22.10b demonstrates the different components of the window chamber frame.

Typically, the tissue thickness ranges from 500 μm to ~1 mm; for tumor experimentation, a bolus of tumor cells is implanted through the underside of the dorsal skinfold. The lifetime of the DSWC is approximately 2–4 weeks, depending on its implantation details and postsurgery care. Figure 22.10 shows typical OCT structural images of the DSWC with and without tumor implantation. The glass cover slip appears transparent, apart from the glass to air/tissue interfaces. The thickness of the dorsal skin tissue can vary significantly, as exemplified in Fig. 22.11a–d. When investigating tumor growth, the cells are left to grow for approximately 1 week before imaging and appear as a tissue mass that bulges out toward the back side of the DSWC, away from the imaging surface (Fig. 22.11c). Proper segmentation of structural OCT images may allow quantitative evaluation of the tumor volume. Some blood vessels may be observed from structural images. Figure 22.11d (arrows) displays large blood vessels whose texture is clearly distinct from the surrounding tissue. The contrast is based on the time-varying speckle pattern of fluids, which causes the region to be smeared out when averaged, whereas static features (solid tissue) would not. When speckle variance signal processing is performed on the 3D data set (22.9), vascular detection down to the capillary level can be observed in the dorsal skin of the window chamber animal model, as seen in Fig. 22.11e.

As such, the DSWC animal model has proven an invaluable tool to allow for an in vivo imaging environment that provides the direct observation of cells, connective tissues, and vascular network. It also provides a continuous longitudinal testing

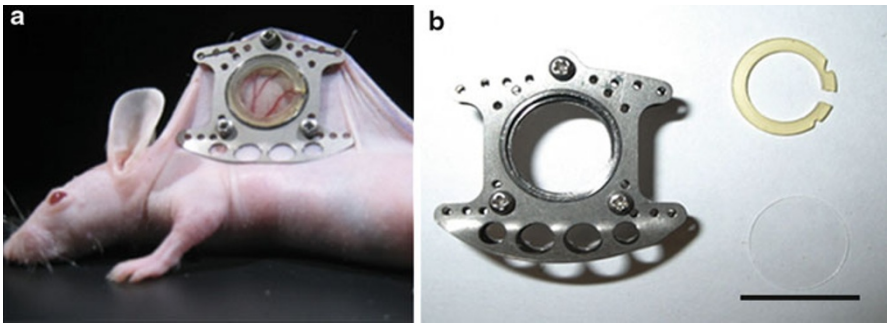

Fig. 22.10 (**a**) A Swiss nude mouse whose dorsal skin had been implanted with a titanium window chamber. (**b**) The titanium chamber, glass cover slip (diameter = 0.8 cm), and plastic fastener are shown. Scale bar = 1 cm

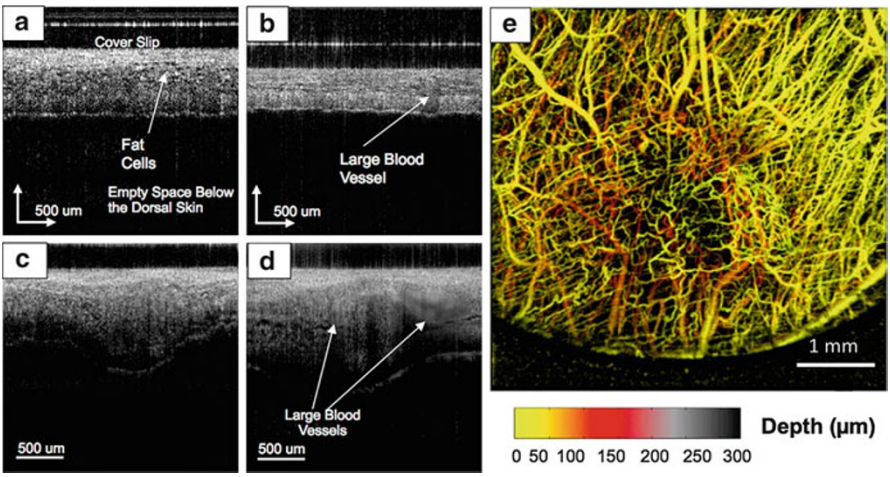

Fig. 22.11 Structural optical coherence tomography images of the dorsal skinfold window chamber from different mice. Each image has a depth of view of 3 mm in air or approximately 2 mm in tissue. (**a**, **b**) Two examples of normal nude mouse skin. (**c**, **d**) Two examples of tumor-bearing nude mouse skin, 1 week posttumor cell implantation. (**a**) Dorsal skin of a nude mouse. The fat cells are visible (labeled). (**b**) Dorsal skin with visible vessel. (**c**) Mouse implanted with ME-180 tumor cells. A tumor mass is present, which manifests as a protrusion on the dermal side of the tissue. (**d**) In another location of the same mouse, prominent blood vessels are seen. (**e**) Speckle variance OCT en face projection image of the mouse dorsal skin, where the colored map indicates the relative depth of the vessels (cf. Fig. 22.7)

environment to optically track and quantify disease progression, cancer therapies, and vascular network development. However, there are several areas of improvement that could further increase the utility of this optical imaging platform. Technically, WC is difficult to implant, requiring specialized surgical tools and frames, and the resulting limited lifetime (1–3 weeks) precluded longer-term observations.

Additionally implanted tumors take on a "pancake" shape, typically 2–4 mm in diameter and ~1–1.5 mm thick. It could be argued that they may not fully represent the physiology of larger tumors in terms of 3D effects, solute transport, and other physiology [80]. Nevertheless, in many cases, the ability to serially image the cellular/vascular/stromal tumor compartments in vivo over extended periods of time (for monitoring disease progression, detailed spatiotemporal response patterns to various types of therapies, etc.) outweighs these disadvantages.

22.5.4 Vascular OCT for Radiation Response Monitoring

Radiation therapy (RT) is one of the most common treatments for cancer. Over half of all cancer patients are treated with RT, either alone or in combination with chemotherapy or surgery [81]. The therapy involves the use of ionizing radiation to kill cancer cells and shrink tumors by primarily damaging their genetic material, which impairs their ability to grow and divide. The therapy is used to treat most types of solid tumors. The radiation dose delivered to each site depends on the location, type, and stage of the cancer, as well as the presence of nearby organs that may be damaged by radiation [82].

RT plays a central role in cancer management. However, its efficacy is also highly influenced by the tumor's surrounding environment or the microenvironment. A nonexhaustive list includes the interaction of tumors with the cells of the immune system and the inflammatory response, oxygen deprivation, and associated signaling molecules [80]. Of particular interest in this chapter is the role of blood vessels.

Development of a functional vascular supply is essential for the successful growth of solid tumors. Typically, existing blood vessels can only support tumor growth to a few millimeters in size before the neoplastic cell population exceeds the nutritional needs [83]. What follows is the initiation of new vascular networks, in a process called angiogenesis [84]. The new blood vessels play several roles for tumor cells: (1) They provide them with nutrients and oxygen for survival, (2) they allow removal of toxic waste from cellular metabolism, and (3) they are the principal route for cancer metastasis [85].

As alluded to previously, tumor blood vessels are very different than that of normal tissues. Structurally, they are chaotic, lack hierarchy, and have an abnormal density. Compositionally, they are incomplete in nature, having missing layers such as basement membranes, endothelial lining, as well as receptors. Tumor endothelial cells also have different phenotypic properties than that of normal vasculature [4]. These characteristics result in vascular networks that are unable to supply sufficient oxygen and nutrient to the tumor mass [86]. Using the window chamber model and custom radiation delivery apparatus, the interplay between tumors and vessels after radiation therapy may be studied with high spatial resolution using OCT.

Here, we present preliminary results that demonstrate the utility of vascular-sensitive OCT in monitoring the vascular changes following a single dose of radiation. The Swiss nude mouse was fitted with a dorsal skinfold window chamber, and tumor cells (ME-180, human cervical carcinoma) were implanted. The tumor

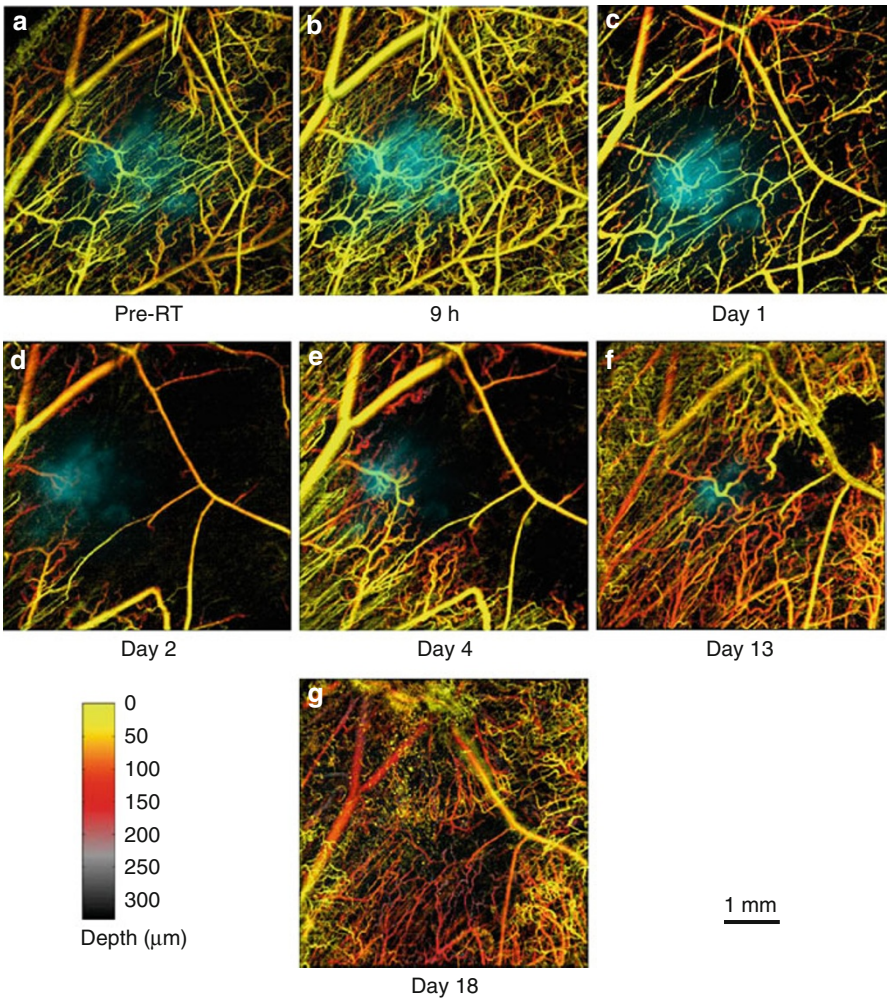

Fig. 22.12 Pseudocolored intravital images demonstrating changes in tumor mass (*cyan-colored*) and vascular architecture (color-coded for depth, see Figs. 22.7 and 22.11e) induced by radiation exposure (30 Gy) using speckle variance OCT and fluorescence microscopy in vivo in the DSWC. The circular treatment region is 4 mm in diameter centered on the tumor. Eight different imaging time points (**a**–**g**) were performed over a period of 18 days. A dramatic decrease in vasculature post-RT occurred within 2 days, followed by gradual revascularization

cells were stably transfected with the DsRed2 fluorescent protein to facilitate the monitoring of in vivo cellular tumor growth by fluorescence microscopy. The nude mouse was treated with single 30 Gy dose of ionizing radiation collimated to the window chamber region and monitored over 18 days. A wide-field fluorescence microscope observed the progression of the tumor, and the vasculature was imaged with speckle variance OCT. Images from both modalities were coregistered to produce the images shown in Fig. 22.12. By day 18, fluorescence signal from the

tumor mass has completely vanished, indicating absence of tumor cells. Most large vessels (arterioles, venules) remained present, but destruction of the majority of the capillaries was observed in day 2, followed by a gradual reperfusion of the tissue.

These OCT vascular results may be used to provide initial feedback or may even predict the long-term efficacy of the radiation therapy treatment as has been the case for other cancer therapies such as PDT studies discussed above [77]. These images may be further processed to obtain quantitative information, such as vascular area or density after skeletonization [87]. With the identification of relevant vascular imaging metrics, these vascular OCT techniques could be used as a feedback mechanism to alter treatment regimes and have the potential to provide individualized patient therapy, based on point-of-care vascular feedback measurements. However, it is important to note that extensive preclinical and clinical testing is required prior to the widespread adoption of OCT vascular monitoring as a means to improve existing radiation therapy treatments.

22.6 Conclusion, Challenges, and Future Outlook

A variety of optical approaches have been developed for structural and functional assessment of intact biological tissues. Of these, OCT is particularly promising owing to its high-micron-scale spatial resolution approaching histological/microscopic levels, portability, relative affordability, and fiber-optic compatibility enabling a variety of clinical scenarios. Further, functional extensions of OCT – spectroscopic, elastographic, polarimetric, textural, Doppler, speckle variance, etc. – allow the acquisition of further useful biological information, often at levels previous inaccessible by other techniques. The latter variants of these extensions, as described in this chapter, are uniquely suited to visualize tissue vasculature at the perfusion and microcirculation levels. Illustrative examples of the utility of microvascular detection and quantification, in the contexts of disease diagnosis and therapeutic monitoring, have been provided.

It is interesting to note that OCT is most often grouped under the "optical diagnostics" rubric of biophotonics, implying its primary role in diagnosis and detection of pathologies. While the important role of early detection and differential diagnosis in oncology cannot be marginalized, there is a growing realization that OCT (and other optical and nonoptical medical imaging techniques) may address other unmet needs in modern medicine. One outstanding opportunity is to provide adjunct information to compliment cancer treatments. Consider radiation therapy and chemotherapy two of the three major weapons at an oncologist's disposal (the other one being surgery). These therapies are essentially blind, in the sense that the success (or failure) of therapy is often not known for weeks or months following their completions, typically assessed by a posttherapy CT or MRI scan. Yet by that time, the delivery of the therapeutic agent, be it ionizing radiation or a chemotherapeutic drug, is over. It would be ideal if some medical imaging or tissue assessment modality could provide feedback on the progress of therapy *during* the course of its delivery so that patient-specific optimization of the

remaining therapeutic regimen could ensue. Such beneficial fusion of diagnostic and therapeutic technologies will clearly benefit patient management (termed "theragnostics" or alternatively "theranostics") and may indeed bring us a step closer to the elusive promise of personalized molecular medicine.

Research in this direction is on the rise. In radiation therapy, while imaging has been widely used for advanced geometric targeting to ensure increased dose conformity (the field of image-guided radiotherapy or IGRT), it is starting to be used for tumor response monitoring as well. Specifically, changes in tumor volume and quantification of tumor shrinkage are starting to be assessed between therapeutic fractions, over the course of a multifractioned radiation delivery. This is a step in the right direction, but clearly, gross anatomical volume changes in the cm^3 range must be preceded by much earlier, more sensitive metrics of radiobiological response. Functional PET studies in radiotherapy patients are also beginning to appear, with the intent of evaluating the changes in the metabolic status of tumors as a result of irradiation [88–90]. But the outstanding issues of resolution, complexity, radiation damage and safety, practicality, and cost are still to be properly addressed.

It is in this context of therapeutic monitoring, feedback, optimization, and "shedding light on therapy" that the vascular OCT techniques discussed in this chapter may have a significant impact. As evidenced by illustrative examples, tissue microvasculature is a sensitive, dynamic, and crucial functional tissue metric that is readily detectable by OCT and may indeed be modulated by a variety of noninvasive therapies such as PDT, chemotherapy, and radiation therapy. The outstanding challenges are many – improve microvascular detectability, quantify the resultant microvascular metrics, test whether the detected blood flow changes are indeed specific to the therapy, determine if these detected changes are indicative of the eventual treatment outcome, and so forth. Some of these challenges have been initially addressed as summarized in this chapter, but clearly much work remains to be done in the exciting field of OCT microvascular imaging.

References

1. R.S. Kerbel, Tumor angiogenesis. N. Engl. J. Med. **358**, 2039–2049 (2008)
2. W. Wang, D. Dean, H. Kaplan, Age-related macular degeneration. Discov. Med. **9**, 13–15 (2010)
3. P.R. Moreno, K. Purushothaman, Neovascularization in human atherosclerosis. Circulation **113**, 2245–2252 (2006)
4. A. Eberhard, S. Kahlert, V. Goede, B. Hemmerlein, K.H. Plate, H.G. Augustin, Heterogeneity of angiogenesis and blood vessel maturation in human tumors: implications for antiangiogenic tumor therapies. Cancer Res. **60**, 1388–1393 (2000)
5. J.R. Less, T.C. Skalak, E.M. Sevick, R.K. Jain, Microvascular architecture in a mammary carcinoma: branching patterns and vessel dimensions. Cancer Res. **51**, 265–273 (1991)
6. C.M.L. West, R.A. Cooper, J.A. Loncaster, D.P. Wilks, M. Bromley, Tumor vascularity: a histological measure of angiogenesis and hypoxia. Cancer Res. **61**, 2907–2910 (2001)
7. S.B. Fox, R.D. Leek, M.P. Weekes, R.M. Whitehouse, K.C. Gatter, A.L. Harris, Quantitation and prognostic value of breast cancer angiogenesis: comparison of microvessel density, Chalkley count, and computer image analysis. J. Pathol. **177**, 275–283 (1995)

8. E. Protopapa, G.S. Delides, L. Revesz, Vascular density and the response of breast carcinomas to mastectomy and adjuvant chemotherapy. Eur. J. Cancer A Gen. Top. **29**, 1391–1393 (1993)
9. E.R. Horak, R. Leek, N. Klenk, S. LeJeune, K. Smith, N. Stuart, M. Greenall, K. Stepniewska, A.L. Harris, Angiogenesis, assessed by platelet/endothelial cell adhesion molecule antibodies, as indicator of node metastases and survival in breast cancer. Lancet **340**, 1120–1124 (1992)
10. H.F. Zhang, K. Maslov, M.-L. Li, G. Stoica, L.V. Wang, In vivo volumetric imaging of subcutaneous microvasculature by photoacoustic microscopy. Opt. Express **14**, 9317–9323 (2006)
11. M.C. Pilatou, N.J. Voogd, F.F.M.D. Mul, W. Steenbergen, L.N.A.V. Adrichem, Analysis of three-dimensional photoacoustic imaging of a vascular tree in vitro. Rev. Sci. Instrum. **74**, 4495–4499 (2003)
12. G. Yu, T. Durduran, C. Zhou, H.W. Wang, M.E. Putt, H.M. Saunders, C.M. Sehgal, E. Glatstein, A.G. Yodh, T.M. Busch, Noninvasive monitoring of murine tumor blood flow during and after photodynamic therapy provides early assessment of therapeutic efficacy. Clin. Cancer Res. **11**, 3543–3552 (2005)
13. C. Menon, G.M. Polin, I. Prabakaran, A. Hsi, C. Cheung, J.P. Culver, J.F. Pingpank, C.S. Sehgal, A.G. Yodh, D.G. Buerk, An integrated approach to measuring tumor oxygen status using human melanoma xenografts as a model. Cancer Res. **63**, 7232–7240 (2003)
14. M.P. Pusztaszeri, W. Seelentag, F.T. Bosman, Immunohistochemical expression of endothelial markers CD31, CD34, von Willebrand factor, and Fli-1 in normal human tissues. J. Histochem. Cytochem. **54**, 385–395 (2006)
15. P. Hsiung, J. Hardy, S. Friedland, R. Soetikno, C. Du, A. Wu, P. Sahbaie, J. Crawford, A. Lowe, C. Contag, Detection of colonic dysplasia in vivo using a targeted heptapeptide and confocal microendoscopy. Nature **14**, 454–458 (2008)
16. A. Meining, D. Saur, M. Bajbouj, V. Becker, E. Peltier, H. HoÃàfler, C.H. von Weyhern, R.M. Schmid, C. Prinz, In vivo histopathology for detection of gastrointestinal neoplasia with a portable, confocal miniprobe: an examiner blinded analysis. Clin. Gastroenterol. Hepatol. **5**, 1261–1267 (2007)
17. M. Khurana, H.A. Collins, E.H. Moriyama, A. Mariampillai, H.L. Anderson, B.C. Wilson, Multi-modality optical imaging of vascular responses to photodynamic therapy in mouse window chamber model. Presented at the BIOMED conference, St. Petersburg, Florida (2008)
18. M. Khurana, E.H. Moriyama, A. Mariampillai, B.C. Wilson, Intravital high resolution optical imaging of individual vessel response to photodynamic treatment. J. Biomed. Opt. **13**, 040502 (2008)
19. A. Fercher, J. Briers, Flow visualization by means of single-exposure speckle photography. Opt. Commun. **37**, 326–330 (1981)
20. J.D. Briers, S. Webster, Laser speckle contrast analysis (LASCA): a nonscanning, full-field technique for monitoring capillary blood flow. J. Biomed. Opt. **1**, 174–179 (1996)
21. Y.C. Huang, T.L. Ringold, J.S. Nelson, B. Choi, Noninvasive blood flow imaging for real-time feedback during laser therapy of port wine stain birthmarks. Lasers Surg. Med. **40**, 167–173 (2008)
22. A.K. Dunn, A. Devor, A.M. Dale, D.A. Boas, Spatial extent of oxygen metabolism and hemodynamic changes during functional activation of the rat somatosensory cortex. Neuroimage **27**, 279–290 (2005)
23. H.K. Shin, A.K. Dunn, P.B. Jones, D.A. Boas, M.A. Moskowitz, C. Ayata, Vasoconstrictive neurovascular coupling during focal ischemic depolarizations. J. Cereb. Blood Flow Metab. **26**, 1018–1030 (2005)
24. H.K. Shin, A.K. Dunn, P.B. Jones, D.A. Boas, E.H. Lo, M.A. Moskowitz, C. Ayata, Normobaric hyperoxia improves cerebral blood flow and oxygenation, and inhibits peri-infarct depolarizations in experimental focal ischaemia. Brain **130**, 1631–1642 (2007)
25. K. Bizheva, A. Unterhuber, B. Hermann, B. Povazay, H. Sattmann, A.F. Fercher, W. Drexler, M. Preusser, H. Budka, A. Stingl, T. Le, Imaging ex vivo healthy and pathological human brain tissue with ultra-high-resolution optical coherence tomography. J. Biomed. Opt. **10**, 11006 (2005)

26. V.X.D. Yang, M.L. Gordon, B. Qi, J. Pekar, S. Lo, E. Seng-Yue, A. Mok, B.C. Wilson, I.A. Vitkin, High speed, wide velocity dynamic range Doppler optical coherence tomography (Part I): system design, signal processing, and performance. Opt. Express **11**, 794–809 (2003)
27. B.J. Vakoc, S.H. Yun, J.F. De Boer, G.J. Tearney, B.E. Bouma, Phase-resolved optical frequency domain imaging. Opt. Express **13**, 5483–5493 (2005)
28. J. Barton, S. Stromski, Flow measurement without phase information in optical coherence tomography images. Opt. Express **13**, 5234–5239 (2005)
29. J. Fingler, D. Schwartz, C. Yang, S.E. Fraser, Mobility and transverse flow visualization using phase variance contrast with spectral domain optical coherence tomography. Opt. Express **15**, 12636–12653 (2007)
30. R.K. Wang, S.L. Jacques, Z. Ma, S. Hurst, S.R. Hanson, A. Gruber, Three dimensional optical angiography. Opt. Express **15**, 4083–4097 (2007)
31. B.J. Vakoc, R.M. Lanning, J.A. Tyrrell, T.P. Padera, L.A. Bartlett, T. Stylianopoulos, L.L. Munn, G.J. Tearney, D. Fukumura, R.K. Jain, B.E. Bouma, Three-dimensional microscopy of the tumor microenvironment in vivo using optical frequency domain imaging. Nat. Med. **15**, 1219–1223 (2009)
32. A. Mariampillai, B.A. Standish, E.H. Moriyama, M. Khurana, N.R. Munce, M.K.K. Leung, J. Jiang, A. Cable, B.C. Wilson, I.A. Vitkin, V.X.D. Yang, Speckle variance detection of microvasculature using swept-source optical coherence tomography. Opt. Lett. **33**, 1530–1532 (2008)
33. C. Kasai, K. Namekawa, A. Koyano, R. Omoto, Real-time two-dimensional blood flow imaging using an autocorrelation technique. IEEE Trans. Sonics Ultrason. **32**, 458–464 (1985)
34. A. Mariampillai, B.A. Standish, N.R. Munce, C. Randall, G. Liu, J.Y. Jiang, A.E. Cable, I.A. Vitkin, V.X.D. Yang, Doppler optical cardiogram gated 2D color flow imaging at 1000 fps and 4D in vivo visualization of embryonic heart at 45 fps on a swept source OCT system. Opt. Express **15**, 1627–1638 (2007)
35. T.C. Chen, B. Cense, M.C. Pierce, N. Nassif, B.H. Park, S.H. Yun, B.R. White, B.E. Bouma, G.J. Tearney, J.F. De Boer, Spectral domain optical coherence tomography ultra-high speed, ultra-high resolution ophthalmic imaging. Arch. Ophthalmol. **123**, 1715–1720 (2005)
36. B.J. Vakoc, G.J. Tearney, B.E. Bouma, Statistical properties of phase-decorrelation in phase-resolved Doppler optical coherence tomography. IEEE Trans. Med. Imaging **28**, 814–821 (2009)
37. V.X.D. Yang, M.L. Gordon, A. Mok, Y. Zhao, Z. Chen, R.S.C. Cobbold, B.C. Wilson, I. Alex Vitkin, Improved phase-resolved optical Doppler tomography using the Kasai velocity estimator and histogram segmentation. Opt. Commun. **208**, 209–214 (2002)
38. H. Ren, Y. Wang, J.S. Nelson, Z. Chen, Power optical Doppler tomography imaging of blood vessel in human skin and M-mode Doppler imaging of blood flow in chick chrioallantoic membrane. *Proceedings of SPIE*, vol. 4956 (2003)
39. L. An, R.K. Wang, In vivo volumetric imaging of vascular perfusion within human retina and choroids with optical micro-angiography. Opt. Express **16**, 11438–11452 (2008)
40. R.K. Wang, Directional blood flow imaging in volumetric optical microangiography achieved by digital frequency modulation. Opt. Lett. **33**, 1878–1880 (2008)
41. G. van Soest, T. Goderie, E. Regar, S. Koljenovi, G. van Leenders, N. Gonzalo, S. van Noorden, T. Okamura, B. Bouma, G. Tearney, Atherosclerotic tissue characterization in vivo by optical coherence tomography attenuation imaging. J. Biomed. Opt. **15**, 011105 (2010)
42. A. Mariampillai, M.K.K. Leung, M. Jarvi, B.A. Standish, K. Lee, B.C. Wilson, A. Vitkin, V.X.D. Yang, Optimized speckle variance OCT imaging of microvasculature. Opt. Lett. **35**, 1257–1259 (2010)
43. A. Mariampillai, Development of a high resolution microvascular imaging toolkit for optical coherence tomography. Thesis from the Department of Medical Biophysics, University of Toronto, Toronto, 2010

44. E.G. Atkinson, S. Jones, B.A. Ellis, D.C. Dumonde, E. Graham, Molecular size of retinal vascular leakage determined by FITC-dextran angiography in patients with posterior uveitis. Eye **5**, 440–446 (1991)
45. J.M. Schmitt, A. Knüttel, Model of optical coherence tomography of heterogeneous tissue. J. Opt. Soc. Am. A Opt. Image Sci. Vis. **14**, 1231–1242 (1997)
46. C. Yang, Molecular contrast optical coherence tomography: a review. Photochem. Photobiol. **81**, 215–237 (2005)
47. L.A. Yannuzzi, J.S. Slakter, J.A. Sorenson, D.R. Guyer, D.A. Orlock, Digital indocyanine green videoangiography and choroidal neovascularization. Retina **12**, 191–223 (1992)
48. U. Morgner, W. Drexler, F.X. Kärtner, X.D. Li, C. Pitris, E.P. Ippen, J.G. Fujimoto, Spectroscopic optical coherence tomography. Opt. Lett. **25**, 111–113 (2000)
49. F. Robles, R.N. Graf, A. Wax, Dual window method for processing spectroscopic optical coherence tomography signals with simultaneously high spectral and temporal resolution. Opt. Express **17**, 6799–6812 (2009)
50. C. Xu, J. Ye, D.L. Marks, S.A. Boppart, Near-infrared dyes as contrast-enhancing agents for spectroscopic optical coherence tomography. Opt. Lett. **29**, 1647–1649 (2004)
51. J.K. Barton, J.B. Hoying, C.J. Sullivan, Use of microbubbles as an optical coherence tomography contrast agent. Acad. Radiol. **9**, S52–S55 (2002)
52. S.A. Boppart, A.L. Oldenburg, C. Xu, D.L. Marks, Optical probes and techniques for molecular contrast enhancement in coherence imaging. J. Biomed. Opt. **10**, 041208 (2005)
53. K.D. Rao, M.A. Choma, S. Yazdanfar, A.M. Rollins, J.A. Izatt, Molecular contrast in optical coherence tomography by use of a pump probe technique. Opt. Lett. **28**, 340–342 (2003)
54. C. Yang, M.A. Choma, L.E. Lamb, J.D. Simon, J.A. Izatt, Protein-based molecular contrast optical coherence tomography with phytochrome as the contrast agent. Opt. Lett. **29**, 1396–1398 (2004)
55. A.L. Oldenburg, V. Crecea, S.A. Rinne, S.A. Boppart, Phase-resolved magnetomotive OCT for imaging nanomolar concentrations of magnetic nanoparticles in tissues. Opt. Express **16**, 11525–11539 (2008)
56. Z. Chen, T.E. Milner, D. Dave, J.S. Nelson, Optical Doppler tomographic imaging of fluid flow velocity in highly scattering media. Opt. Lett. **22**, 64–66 (1997)
57. J.A. Izatt, M.D. Kulkarni, S. Yazdanfar, J.K. Barton, A.J. Welch, In vivo bidirectional color Doppler flow imaging of picoliter blood volumes using optical coherence tomography. Opt. Lett. **22**, 1439–1441 (1997)
58. S. Yazdanfar, A.M. Rollins, J.A. Izatt, Imaging and velocimetry of the human retinal circulation with color Doppler optical coherence tomography. Opt. Lett. **25**, 1448–1450 (2000)
59. S. Makita, Y. Hong, M. Yamanari, T. Yatagai, Y. Yasuno, Optical coherence angiography. Opt. Express **14**, 7821–7840 (2006)
60. J.S. Schuman, C.A. Puliafito, J.G. Fujimoto, *Optical Coherence Tomography of Ocular Diseases* (Slack, Thorofare, NJ, 2004)
61. V. Gupta, A. Gupta, M. Mangat Ram Dogra, *Atlas Optical Coherence Tomography of Macular Diseases and Glaucoma* (Jaypee Brothers Medical, New Delhi, India, 2010)
62. Y. Wang, A.A. Fawzi, R. Varma, A.A. Sadun, X. Zhang, O. Tan, J.A. Izatt, D. Huang, Pilot study of optical coherence tomography measurement of retinal blood flow in retinal and optic nerve diseases. Invest. Ophthalmol. Vis. Sci. **52**, 840–845 (2011)
63. T.J. Dougherty, C.J. Gomer, B.W. Henderson, G. Jori, D. Kessel, M. Korbelik, J. Moan, Q. Peng, Photodynamic therapy. J. Natl. Cancer Inst. **90**, 889–905 (1998)
64. Z. Huang, A review of progress in clinical photodynamic therapy. Technol. Cancer Res. Treat. **4**, 283–293 (2005)
65. Z. Luksiene, Photodynamic therapy: mechanism of action and ways to improve the efficiency of treatment. Medicina (Kaunas) **39**, 1137–1150 (2003)
66. M.S. Patterson, S.J. Madsen, B.C. Wilson, Experimental tests of the feasibility of singlet oxygen luminescence monitoring in vivo during photodynamic therapy. J. Photochem. Photobiol. B Biol. **5**, 69–84 (1990)

67. C.M. Moore, I.M. Hoh, S.G. Bown, M. Emberton, Does photodynamic therapy have the necessary attributes to become a future treatment for organ-confined prostate cancer? BJU Int. **96**, 754–758 (2005)
68. G. Volden, T. Christensen, J. Moan, Photodynamic membrane damage of hematoporphyrin derivative-treated NHIK 3025 cells in vitro. Photobiochem. Photobiophys. **3**, 105–111 (1981)
69. J. Moan, J. McGhie, P.B. Jacobsen, Photodynamic effects on cells in vitro exposed to hematoporphyrin derivative and light. Photochem. Photobiol. **37**, 599–604 (1983)
70. K.G. Specht, M.A. Rodgers, Depolarization of mouse myeloma cell membranes during photodynamic action. Photochem. Photobiol. **51**, 319–324 (1990)
71. A. Ketabchi, A. MacRobert, P.M. Speight, J.H. Bennett, Induction of apoptotic cell death by photodynamic therapy in human keratinocytes. Arch. Oral Biol. **43**, 143–149 (1998)
72. G. Buggiani, M. Troiano, R. Rossi, T. Lotti, Photodynamic therapy: off-label and alternative use in dermatological practice. Photodiagnosis Photodyn. Ther. **5**, 134–138 (2008)
73. D. Fukumura, R.K. Jain, Tumor microvasculature and microenvironment: targets for anti-angiogenesis and normalization. Microvasc. Res. **74**, 72–84 (2007)
74. B. Chen, C. He, P. de Witte, P.J. Hoopes, T. Hasan, B.W. Pogue, Vascular targeting in photodynamic therapy, in *Advances in Photodynamic Therapy: Basic, Translational, and Clinical*, ed. by M.R. Hamblin, P. Mroz (Artech House, Norwood, 2008), pp. 179–191
75. V.X.D. Yang, Y.X. Mao, N. Munce, B. Standish, W. Kucharczyk, N.E. Marcon, B.C. Wilson, I.A. Vitkin, Interstitial Doppler optical coherence tomography. Opt. Lett. **30**, 1791–1793 (2005)
76. B.A. Standish, X. Jin, J. Smolen, A. Mariampillai, N.R. Munce, B.C. Wilson, I.A. Vitkin, V.X.D. Yang, Interstitial Doppler optical coherence tomography monitors microvascular changes during photodynamic therapy in a Dunning prostate model under varying treatment conditions. J. Biomed. Opt. **12**, 034022 (2007)
77. B. Standish, K. Lee, X. Jin, A. Mariampillai, N. Munce, M. Wood, B. Wilson, I. Vitkin, V. Yang, Interstitial Doppler optical coherence tomography as a local tumor necrosis predictor in photodynamic therapy of prostatic carcinoma: an in vivo study. Cancer Res. **68**, 9987–9995 (2008)
78. J.C. Sandison, The transparent chamber of the rabbit's ear giving a complete description of improved techniques of construction and introduction and general account of growth and behavior of living cells and tissues as seen with the microscope. Am. J. Anat. **41**, 447–472 (1928)
79. G.E. Koehl, A. Gaumann, E.K. Geissler, Intravital microscopy of tumor angiogenesis and regression in the dorsal skin fold chamber: mechanistic insights and preclinical testing of therapeutic strategies. Clin. Exp. Metastasis **26**, 329–344 (2009)
80. M.W. Dewhirst, Y. Cao, B. Moeller, Cycling hypoxia and free radicals regulate angiogenesis and radiotherapy response. Nat. Rev. Cancer **8**, 425–437 (2008)
81. J.B. Owen, L.R. Coia, G.E. Hanks, Recent patterns of growth in radiation therapy facilities in the United States: a patterns of care study report. Int. J. Radiat. Oncol. Biol. Phys. **24**, 983–986 (1992)
82. B. Emami, J. Lyman, A. Brown, L. Coia, M. Goitein, J.E. Munzenrider, B. Shank, L.J. Solin, M. Wesson, Tolerance of normal tissue to therapeutic irradiation. Int. J. Radiat. Oncol. Biol. Phys. **21**, 109–122 (1991)
83. D.W. Siemann, M.R. Horsman, Chapter 8 – Significance of the tumour microenvironment in radiotherapy, in *Cancer Microenvironment and Therapeutic Implications*, ed. by G. Baronzio, G. Fiorentini, C.R. Cogle (Springer, 2009)
84. J. Folkman, Angiogenesis in cancer, vascular, rheumatoid and other disease. Nat. Med. **1**, 27–31 (1995)
85. O. Stöltzing, L.M. Ellis, The role of microvasculature in metastasis formation, in *Vascular-Targeted Therapies in Oncology*, ed. by D.W. Siemann (Wiley, Chichester, 2006), pp. 31–62
86. P. Vaupel, Tumor microenvironmental physiology and its implications for radiation oncology. Semin. Radiat. Oncol. **14**, 198–206 (2004)

87. T.C. Lee, R.L. Kashyap, C.N. Chu, Building skeleton models via 3-D medial surface axis thinning algorithms. CVGIP: Graph. Model Image Process. **56**, 462–478 (1994)
88. I. Madani, W. Duthoy, C. Derie, W. De Gersem, T. Boterberg, M. Saerens, F. Jacobs, V. Grégoire, M. Lonneux, L. Vakaet, B. Vanderstraeten, W. Bauters, K. Bonte, H. Thierens, W. De Neve, Positron emission tomography-guided, focal-dose escalation using intensity-modulated radiotherapy for head and neck cancer. Int. J. Radiat. Oncol. Biol. Phys. **68**, 126–135 (2007)
89. T. Gupta, S. Jain, J.P. Agarwal, V. Rangarajan, N. Purandare, S. Ghosh-Laskar, K.A. Dinshaw, Diagnostic performance of response assessment FDG-PET/CT in patients with head and neck squamous cell carcinoma treated with high-precision definitive (chemo)radiation. Radiother. Oncol. **97**, 194–199 (2010)
90. D.S. Yoo, T.Z. Wong, D.M. Brizel, The role of adaptive and functional imaging modalities in radiation therapy: approach and application from a radiation oncology perspective. Semin. Ultrasound CT MRI **31**, 444–461 (2010)